THE JOURNAL OF PHYSICAL CHEMISTRY C
A JOURNAL OF THE AMERICAN CHEMICAL SOCIETY

pubs.acs.org/JPCC

Article

Toward High Luminescence Dissymmetry Factor in Circularly Polarized MR-TADF Emitters via Multi-Strategy Optimization: A Computational Study

Ramalingam Mahaan, Weitang Li, and Zhigang Shuai*

Cite This: *J. Phys. Chem. C* 2026, 130, 7812−7825

Read Online

ACCESS | Metrics & More | Article Recommendations | Supporting Information

ABSTRACT: Circularly polarized multiple-resonance thermally activated delayed fluorescence (CP-MR-TADF) emitters have gained immense interest in advanced optoelectronics due to their unique combination of narrow emission, efficient TADF, and chirality. However, their rational design requires a deeper understanding of the intricate structure-property relationships that govern their photophysical and chiroptical behavior. In this work, we systematically explore a series of helicene-based CP-MR-TADF emitters through four strategic modifications: the core framework (B-N-B vs. N-B-N), MR-TADF skeleton architecture, chiral unit variation, and the heavy-atom effect (O, S, Se). Employing high-level STEOM-DLPNO-CCSD calculations benchmarked against experimental data, we theoretically design 28 novel molecules to target highly efficient CPL properties and accurately predict excited-state energies. Our analysis reveals that the B-N-B framework consistently yields superior color purity, with FWHM values as narrow as ∼14 nm, resulting from minimized structural relaxation. The incorporation of heavy atoms (O, S, Se) systematically enhances reverse intersystem crossing (RISC) rates up to $\sim 10^7$ s^{-1} by strengthening SOC and reducing the ΔE_{ST} gap, making it ideally suited for the TADF process. All designed molecules exhibit high luminescence dissymmetry factors on the order of $\sim 10^{-3}$, with the N-B-N framework yielding the maximum values, up to 4.17×10^{-3}, attributed to its characteristic enhanced transition electric-magnetic dipole moment angles. Notably, the N-B-N framework significantly increases the racemization barrier by ∼20 kcal mol^{-1} relative to the B-N-B framework, thereby ensuring configurational stability under ambient conditions. This study establishes clear structure-property relationships and outlines a design framework for developing high-performance CP-MR-TADF emitters with balanced narrow-width emission, efficient triplet harvesting, and strong chiroptical activity.

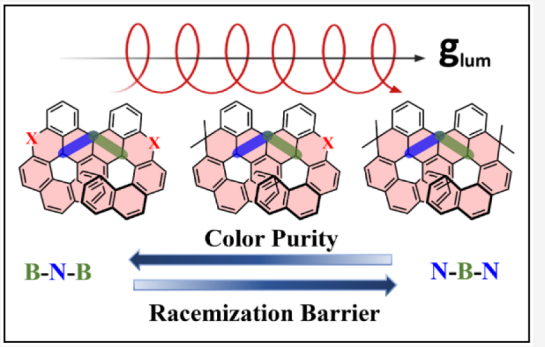

KEYWORDS: *CP-MR-TADF, helicity, color purity, g_{lum}, racemization barrier*

1. INTRODUCTION

Circularly polarized luminescence (CPL) has drawn considerable research interest in recent years owing to its potential for enabling applications in CPL organic light-emitting diodes (OLEDs), three-dimensional displays, data storage, biological sensing, and other fields.[1,2] In general, CPL light is a combination of two linearly polarized lights with a $\lambda/4$ phase difference, maintaining constant electric vector amplitude while uniformly changing the propagation over time, where counterclockwise rotation corresponds to right-hand CPL and clockwise rotation to left-hand CPL light. In conventional optoelectronic devices, particularly OLEDs, CPL light is typically generated by achiral emitters through an anti-glare filter system comprising a quarter-wave plate and a linear polarizer. This approach inherently compromises ∼50% of the device's energy and adds unnecessary complexity.[3] Consequently, it is imperative to develop new chiral emitters that can directly produce CPL light, with their efficiency measured by the luminescence dissymmetry factor, denoted as g_{lum}. Initial efforts to achieve high g_{lum} in CPL emitters predominantly used f-block lanthanide and d-block transition-metal complexes, as these systems inherently support robust magnetic-dipole transitions.[4] The highest g_{lum} value reported to date is approximately 1.41, achieved in a cesium complex.[5] Nonetheless, their low quantum yields and the practical difficulties in modifying and processing lanthanide and metal complexes pose major obstacles to their adoption in optoelectronic applications.[6] Chiral metal-free organic luminescent emitters, with their precise molecular structures, high quantum yields, easy functionalization, and simple post-

Published: May 15, 2026

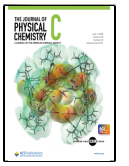

https://doi.org/10.1021/acs.jpcc.6c01502
J. Phys. Chem. C 2026, 130, 7812−7825

processing, are highly promising for CPL research.[7] The g_{lum}, which is defined as:

$$g_{lum} = 4\cos\theta \frac{|\mu_m||\mu_e|}{|\mu_m|^2 + |\mu_e|^2}$$

Here, $|\mu_m|$, and $|\mu_e|$ represent the transition magnetic (MDM) and electric dipole moments (EDM), respectively, with theta (θ) being the angle between them. Achieving a high g_{lum}, which can reach a theoretical maximum of |2|, requires a chiral emitter to maximize $|\mu_m|$, and while minimizing $|\mu_e|$ and to align θ such that the two moments are either parallel or antiparallel. However, in most organic molecules, the magnitude of the MDM is often significantly smaller and frequently negligible compared to that of the EDM, which poses a fundamental limitation.[8] Therefore, a high g_{lum} can only be attained through the synergetic control of the MDM, the EDM, and their relative orientation of θ.

Light-emitting materials in OLEDs have progressed from first-generation fluorescence to second-generation phosphorescence and third-generation thermally activated delayed fluorescence (TADF) emitters, each with unique advantages and limitations.[9−11] Currently, TADF and multiple-resonance TADF (MR-TADF) emitters are demonstrating the potential to achieve 100% internal quantum efficiency (IQE) while relying exclusively on organic components.[12] However, traditional TADF emitters often produce broad full-width at half maximum (FWHM > 40 nm) due to limited conjugation between donor (D) and acceptor (A) units, which compromises color purity.[13] To overcome this limitation, MR-TADF emitters with rigid molecular skeletons were developed, where the D and A atoms are strategically positioned to induce a spatially separated distribution of the highest occupied molecular orbital (HOMO) and the lowest unoccupied molecular orbital (LUMO). This design enables narrowband emission (FWHM < 40 nm), which is essential for achieving high color purity and efficiency.[14] Harnessing these advantages, MR-TADF emitters have emerged as ideal candidates for generating CPL, as they can simultaneously exhibit both CPL and efficient TADF properties. Therefore, employing an intrinsically helical framework represents a promising optimization strategy for designing high-performance CP-MR-TADF emitters.[3]

Recent experimental and theoretical progress has identified promising candidates for CP-MR-TADF emitters in OLEDs, which exhibit high quantum efficiency, narrow-band emission, and significant g_{lum} values.[15−19] In 2022, Wu *et al.* reported a series of CP-MR-TADF emitters based on asymmetrical peripheral locking, the heavy-atom effect, and symmetry-breaking strategies to enhance g_{lum} in B/N-doped [4]-helicenes.[20] The BN5 emitter achieved a g_{lum} value on the order of $1.0-2.0\times10^{-3}$. In the same year, Yang *et al.* developed an M-shaped double hetero[5]-helicene by extending a [4]-helicene-BN3 core into a [5]-helicene-BN system, enhancing its chiral properties.[21] This emitter demonstrated a high g_{lum} of approximately 2.0×10^{-3} and a higher racemization barrier than the BN5 and BN3 analogues. Notably, both BN5, BN3, and [5]-helicene-BN emitters share the structural framework of an N-B-N core. In 2023, Zhang *et al.* reported very narrowband CPL emitters employing single and double [7]-helicene structures, demonstrating the advantage of double helicenes over single helicenes within an MR-TADF core.[22] More recently, Ye *et al.* introduced narrowband hetero[6]-helicenes with a B-N-B framework, doped at the chiral unit with oxygen (DB-O) and sulfur (DB-S). This approach successfully increased the g_{lum} values to 1.4×10^{-3} and 1.5×10^{-3}, respectively, with corresponding narrow FWHM of 24 nm and 23 nm.[23] Despite considerable progress in enhancing g_{lum} values, the design of helicity-based CP-MR-TADF emitters lacks a comprehensive framework that reliably connects molecular architecture and its precise functionalization to key photophysical and chiroptical performance, underscoring the need for a more systematic design strategy and investigation. In this work, we perform a comprehensive theoretical investigation of how (i) the molecular framework (B-N-B vs. N-B-N), (ii) MR-TADF core architecture, (iii) helicity, and (iv) the heavy-atom effect collectively govern the properties of MR-TADF emitters. Inspired by recent experimental and computational findings on CP-MR-TADF design,[20−24] we extend this design paradigm to systematically explore the optical and chiral properties of a newly designed system via distinct strategic modifications, using high-level quantum-chemical calculations.

2. COMPUTATIONAL DETAILS

The selection of appropriate computational methodologies for determining the ground- and excited-state properties of MR-TADF emitters is crucial. In this study, we have selected commonly utilized MR-TADF skeletons and their heteroatom-doped derivatives to perform a detailed benchmark study analysis (Tables S1−S2 and Figures S1−S2). The ground state geometries of these MR-TADF derivatives (BN1, BN3, BNSeSe, BN5, and DMAC-BN)[20,25,26] were optimized using the B3LYP functional, which has also been widely employed in the design of numerous TADF and MR-TADF emitters.[27−29] Notably, we obtained HOMO energies for three of five experimentally reported molecules, and the calculated HOMO energies of these MR-TADF derivatives are in good agreement with the experimentally determined values, with a mean absolute deviation (MAD) of 0.01 eV (Figure S1b). Based on these findings, the B3LYP functional was selected for the ground state optimization of the newly designed CP-MR-TADF emitters in this work.

To conduct the excited-state benchmark studies, we used two established methodologies to predict the excited-state energies of MR-TADF emitters. In 2022, Pratik *et al.* reported the design of sulfur and selenium atom-containing MR-TADF emitters using the state-specific equation of motion-domain local pair natural orbital coupled-cluster singles and doubles (STEOM-DLPNO-CCSD) method, which showed good accuracy in predicting the excited-state energies of MR-TADF emitters.[30,31] More recently, Sanyam *et al.* studied that the double hybrid B2PLYP functional is a cost-effective approach for modeling MR-TADF emitter design, yielding results that are in good agreement with those obtained using the computationally expensive STEOM-DLPNO-CCSD method.[32] We successfully obtained the experimental singlet (S_1) and triplet (T_1) values for three out of the five molecules and the S_1-T_1 gap (ΔE_{ST}) values for all five molecules. The MAD of the S_1 values (MAD ranging from 0.19 to 0.13 eV) and T_1 values (MAD ranging from 0.14 to 0.08 eV) decreased progressively from the B2PLYP to the STEOM-DLPNO-CCSD method (Figure S1c and Table S3). Meanwhile, the ΔE_{ST} values predicted by the two methods, B2PLYP and STEOM-DLPNO-CCSD, were comparable, with MAD of about 0.07 and 0.06 eV, respectively (Figure S2). Our findings suggest that the STEOM-DLPNO-CCSD method provides

https://doi.org/10.1021/acs.jpcc.6c01502
J. Phys. Chem. C 2026, 130, 7812−7825

robust predictions for all S_1, T_1, and ΔE_{ST} values. However, the B2PLYP functional, which is more cost-effective than the computationally intensive STEOM-DLPNO-CCSD method, offers a viable alternative while maintaining good accuracy. Initially, we employed the B2PLYP functional to perform excited-state calculations for our newly designed molecules. However, we encountered two significant limitations with this approach. Firstly, some molecules exhibited negative ΔE_{ST} gaps, even when the Tamm−Dancoff approximation (TDA) was included within the time-dependent density functional theory (TD-DFT) formalism. Secondly, the B2PLYP functional does not support spin-orbit coupling (SOC) calculations. These limitations precluded further progress with the B2PLYP functional. Consequently, we opted to calculate the excited-state energies of all newly designed molecules using the STEOM-DLPNO-CCSD method.

The radiative decay rate is calculated using the Einstein spontaneous emission formula[33]

$$k_r = \frac{f\Delta E_{fi}^2}{1.499}$$

Here, f denotes the dimensionless oscillator strength of the initial S_1 state, ΔE_{fi} is the energy between S_1 and the ground state (S_0) expressed in cm^{-1} so that k_r is in units of s^{-1}.[34] A semi-classical Marcus equation was utilized to calculate the rate of reverse intersystem crossing (RISC) between the excited states.[35,36]

$$k = \frac{|V|^2}{\hbar^2}\left(\frac{\pi}{\lambda k_B T}\right)^{1/2} \exp\left[-\frac{(\Delta G + \lambda)^2}{4\lambda k_B T}\right]$$

Here, k_B denotes the Boltzmann constant, T represents the temperature, which is approximately 300 K. The SOC prefactor V, was calculated using the STEOM-DLPNO-CCSD method. To provide an accurate model of the system, contributions from both the T_1 and T_2 states, weighted by Boltzmann thermal populations,[37] were included in the calculation of the RISC rate for cases where the higher triplet states lie below S_1 (further details are provided in the Supporting Information). The B3LYP functional is known to overemphasize charge transfer (CT) characteristics in MR-TADF systems, making it suboptimal for accurately describing their short-range CT (SRCT) nature. To better model SRCT, we adopted the range-separated CAM-B3LYP functional.[38] With this approach, the calculated FWHM was about 46.59 nm, which is in excellent agreement with the experimental value of 46 nm reported for [5]-helicene-BN CPL emitter (Table S4).[21] The FWHM, Huang-Rhys (HR) factors, and frequency analysis were computed using the thermal vibration correlation function (TVCF) method, as implemented in our in-house MOMAP package.[33,39−41] The transition EDM and MDM densities, the electronic circular dichroism (ECD) spectrum, and the decomposition of the EDM and MDM vectors were analyzed using the Multiwfn package.[42] For the chiroptical properties, we employed the CAM-B3LYP functional for an in-depth analysis. For CP-MR-TADF emitters, the racemization energy barrier is imperative for assessing synthetic stability. Therefore, we used the M06-2X functional for energy barrier calculations, as it is parameterized to include correlation effects that mimic dispersion, a vital feature for transition-state calculations.[43] The B3LYP, M06-2X, and CAM-B3LYP calculations were carried out using Gaussian 16,[44] while the STEOM-DLPNO-CCSD and B2PLYP calculations were conducted using ORCA 6.0.1 software.[45] All calculations were carried out in the gas phase medium, employing the def2-SVP basis set.

3. MOLECULAR SELECTION AND DESIGN STRATEGY

Given the numerous MR-TADF emitters reported to date, evaluating all possible skeletons presents a significant challenge. To address this, we selected three representative skeletons, named skeletons 1, 2, and 3 (Figure 1). In skeleton

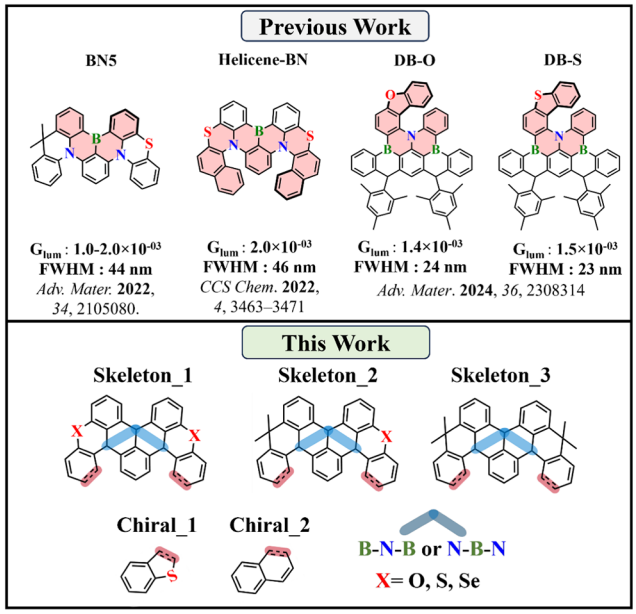

Figure 1. Chemical structures of previously reported representative examples, and molecular design strategy for CP-MR-TADF emitters in this work.

1, bridging heteroatoms on both sides form a rigid locked ring. This design plays a crucial role in enhancing inter-system crossing (ISC) and RISC rates via the heavy-atom effect and also facilitates chiral separation by increasing helical curvature induced by the bridging atoms. In skeleton 2, we introduced a dangling methylene-substituted unit on one side, which forms intramolecular flexible lockers to improve the solubility of the target molecules. Importantly, this peripheral lock disrupts the molecular symmetry. Skeleton 3 contains only a methylene-substituted intramolecular locker on both sides without heteroatom doping sites and regains symmetry, similar to skeleton 1. Within these three skeletons, we adopted two distinct frameworks: B-N-B and N-B-N, resulting in a total of six skeletons named A(X), B(X), C(X), D(X), E, and F (Figure 2). Here, X represents the heteroatom, oxygen (O), sulfur (S), or selenium (Se), as illustrated in Figure 2. Skeletons A(X), C(X), and E belong to the B-N-B family, while skeletons B(X), D(X), and F belong to the N-B-N family. These six skeletons yield a total of 28 derivatives through heteroatom doping: the first four skeletons (A(X), B(X), C(X), and D(X)) each produce three derivatives (varying X), whereas skeletons E and F each yield one derivative. While helicenes composed exclusively of carbon and hydrogen have traditionally been the focus of chirality studies, recent progress has been driven by the advent of hetero-helicenes.[46] These systems incorporate heteroatoms such as

https://doi.org/10.1021/acs.jpcc.6c01502
J. Phys. Chem. C 2026, 130, 7812−7825

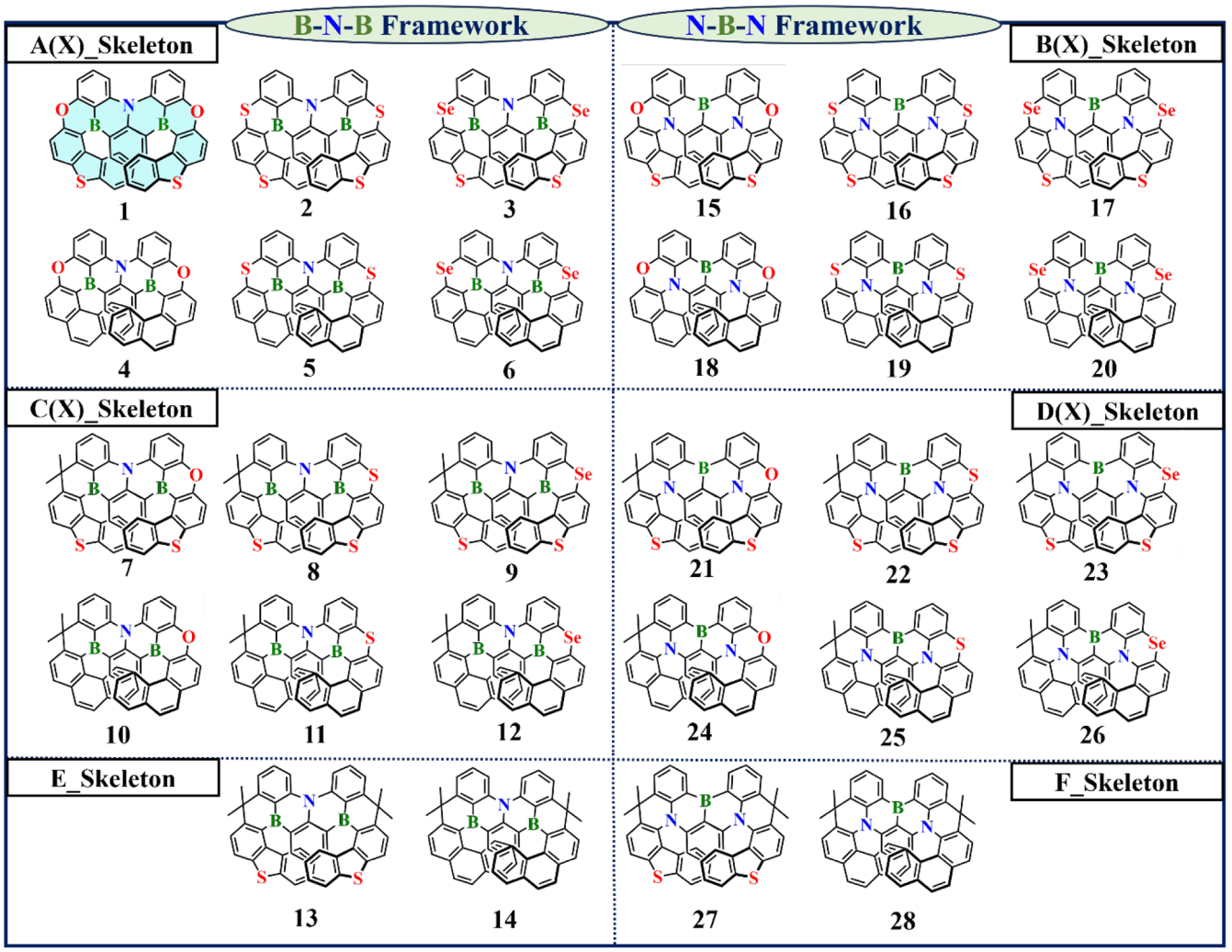

Figure 2. Chemical structures of the newly designed CP-MR-TADF molecules.

oxygen, boron, sulfur, and nitrogen to better tailor chiroptical properties. In this study, we extend our investigations to include a sulfur-atom-containing heterohelicene, along with the conventional one. The comprehensive molecular design encompassing the MR-TADF units, CPL units, and the final CP-MR-TADF molecules is depicted in Figures 1−2. As shown in Figure 2, this study designed 28 CP-MR-TADF emitters. These emitters are classified according to four distinct design strategies: (i) **Framework** (B-N-B and N-B-N): Molecules 1−14 belong to the B-N-B framework, while molecules 15−28 belong to the N-B-N framework. (ii) **MR-TADF Skeletons** 1, 2, and 3. (iii) **Chiral Units** 1 and 2. (iv) **Heavy-Atom Effect** for skeletons 1 and 2 (O, S, and Se).

4. RESULTS AND DISCUSSION

4.1. Color Purity

The color purity of OLED emitters is fundamentally determined by two key factors: structural relaxation and vibronic-coupling characteristics. To investigate the structure-property relationships and the mechanistic roles of four strategies in shaping FWHM, we systematically analyzed the electronic structures and vibrational properties of all newly designed CP-MR-TADF emitters. To evaluate this, we calculated the total reorganization energies between the S_1 and S_0 states (Table S5 and Figures 3, S3−S4). Generally, high and low reorganization energies correspond to broader and narrower bandwidths, respectively. The B-N-B framework-based molecules exhibit a narrow FWHM, ranging from 14.45 to 18.40 nm. In contrast, the N-B-N framework yields a slightly broader bandwidth of 18.58−36.92 nm. This difference is due to the higher reorganization energies of the N-B-N emitters (715.88−1439.78 cm^{-1}) compared to the B-N-B emitters (512.43−651.08 cm^{-1}). In particular, modifying the MR-TADF skeleton, chiral unit, or heavy atoms has a smaller effect on the bandwidth than the choice between B-N-B and N-B-N frameworks. The heavy-atom effect slightly increases the FWHM from O to S to Se with increasing atomic radius in the B-N-B frameworks, while in the N-B-N frameworks, it increases from O to S but decreases from S to Se. This trend correlates with their total reorganization energies and suggests that the heavy-atom effect is framework-dependent. Notably, the linear correlation between FWHM and total reorganization energies, shown in Figure 3b, yields an R^2 value of 0.96, demonstrating a strong relationship between these two quantities. However, for molecules 1−3, the FWHM values increase with the heavy-atom effect, even though their reorganization energies decrease, highlighting that additional factors may influence the bandwidth of these emitters. Therefore, we calculated the vibronic coupling between

https://doi.org/10.1021/acs.jpcc.6c01502
J. Phys. Chem. C 2026, 130, 7812−7825

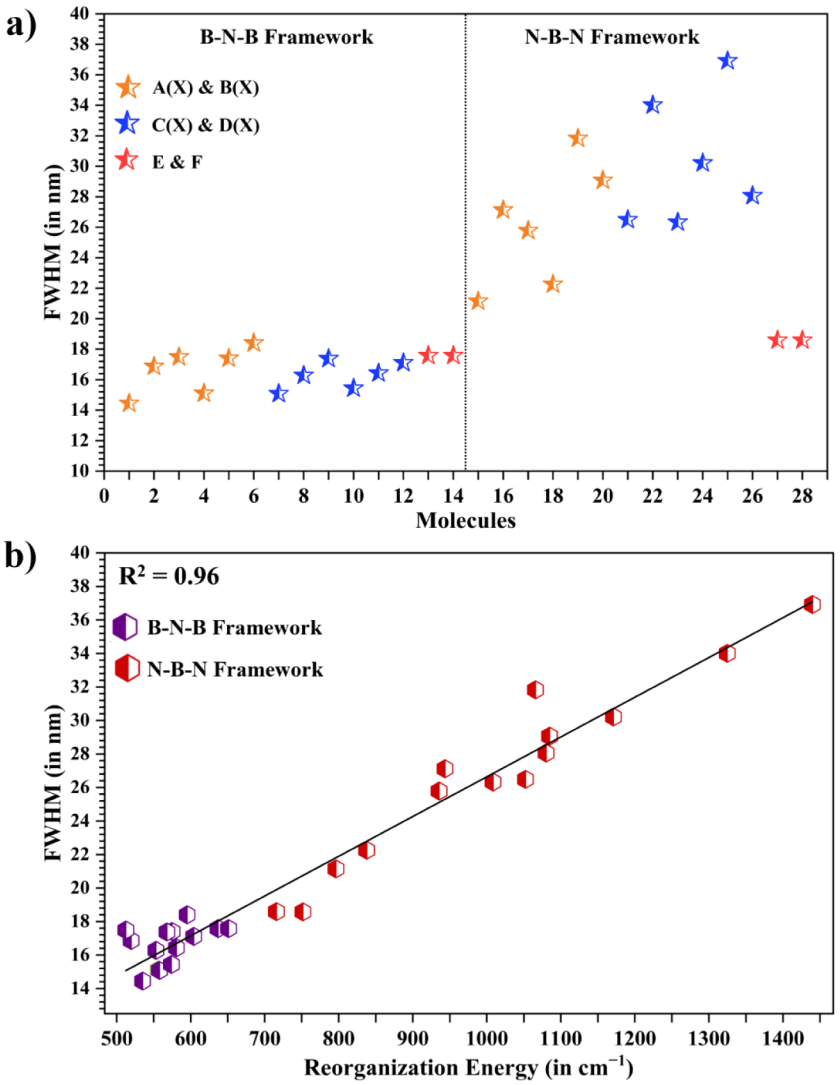

Figure 3. FWHM of newly designed molecules (a), correlation diagram between FWHM and reorganization energy (b).

electronic states and vibrational transitions to investigate the cause of this discrepancy, using Huang-Rhys (HR) factors. As shown in Table S5 and Figure S3, the HR factors for molecules 1−3 increase from 1.66 to 2.45 to 2.72, which accounts for the increase in FWHM. Importantly, N-B-N framework-based emitters exhibited lower HR factor values than their B-N-B counterparts, yet still produced a broader bandwidth. The weak coupling observed between electronic and vibrational transitions in the B-N-B framework emitter is evidenced by its dominant vibrational modes, all of which reside in the low-frequency region below 100 cm^{-1} (Figure S3). In contrast to B-N-B emitters, N-B-N frameworks exhibit a broader emission spectrum due to the induction of additional vibrational modes spanning both the low-frequency (<100 cm^{-1}) and high-frequency (~200 to ~800 cm^{-1}) regions, which collectively reduce the color purity even with a low HR value (Figure S4). More importantly, all designed molecules exhibited enhanced color purity (FWHM = 14.45−36.92 nm) compared to the experimentally reported 5-Helicene-BN emitter (FWHM = 46 nm). Notably, the tuned versions, such as the modified extended helicene and chiral unit-changed molecules 19 and 16, significantly improved FWHMs of 31.83 nm and 27.12 nm, respectively, compared to the Helicene-BN emitter. This improvement correlates with a substantial reduction in their reorganization energies from 1872.02 cm^{-1} (5-Helicene-BN) to 1065.84 cm^{-1} (19) to 943.34 cm^{-1} (16) and the corresponding HR factors. Based on the color purity analysis, the following points can be drawn: (i) The B-N-B framework favors a narrower emission spectrum than the N-B-N framework. (ii) Modifications to the MR-TADF cores and altering the chiral units slightly affect color purity. In contrast to the MR-TADF skeleton 3, both the B-N-B and N-B-N motifs had a similar effect, yielding a similar narrow FWHM of ~18 nm, and suggest that the MR-TADF skeleton 3 is framework- and chiral unit-independent. (iii) The heavy-atom effect (changing O to S to Se) slightly broadens the spectrum in the B-N-B framework (~2 nm increase). In the N-B-N framework, however, the effect is more significant: the spectrum broadens considerably from O to S but narrows from S to Se. These spectral changes arise from differences in structural relaxation between the S_1 and S_0 states, which correlate strongly with reorganization energies and vibrational modes.

4.2. TADF Properties

The excited state properties, including S_1, T_n, ΔE_{ST}, oscillator strength (f), radiative rate (k_r), SOC, and RISC rates, are

https://doi.org/10.1021/acs.jpcc.6c01502
J. Phys. Chem. C 2026, 130, 7812−7825

Table 1. Calculated Singlet and Triplet Energies, Singlet (S_1)-Triplet (T_1) Energy Differences (ΔE_{ST}in eV), Oscillator Strength (f), SOC Magnitudes (in cm^{-1}), Radiative Decay (k_r) (in s^{-1}), and RISC Rates (in s^{-1})

						SOC				
Mol.	S_1	T_1	T_2	ΔE_{ST}	f	S_1-T_1	S_1-T_2	S_1-T_3	k_r	RISC
1	2.57	2.43	2.43	0.14	0.42	0.16	0.16	0.18	$1.21 \times 10^{+8}$	$7.66 \times 10^{+4}$
2	2.44	2.32	2.57	0.12	0.36	0.07	0.11	0.05	$9.43 \times 10^{+7}$	$3.71 \times 10^{+4}$
3	2.44	2.32	2.57	0.11	0.37	0.69	5.99	4.15	$9.49 \times 10^{+7}$	$5.32 \times 10^{+6}$
4	2.70	2.55	2.56	0.15	0.39	0.14	0.13	0.05	$1.23 \times 10^{+8}$	$4.40 \times 10^{+4}$
5	2.54	2.42	2.66	0.12	0.36	0.58	1.00	0.44	$1.01 \times 10^{+8}$	$2.54 \times 10^{+6}$
6	2.54	2.42	2.62	0.13	0.35	1.32	7.73	0.35	$9.82 \times 10^{+7}$	$8.56 \times 10^{+6}$
7	2.61	2.48	2.76	0.13	0.38	0.18	0.51	0.20	$1.14 \times 10^{+8}$	$1.68 \times 10^{+5}$
8	2.52	2.39	2.73	0.14	0.36	0.47	1.27	1.33	$1.01 \times 10^{+8}$	$7.01 \times 10^{+5}$
9	2.48	2.38	2.55	0.10	0.35	1.12	3.59	4.29	$9.29 \times 10^{+7}$	$1.75 \times 10^{+7}$
10	2.65	2.38	2.50	0.27	0.35	0.05	0.17	0.14	$1.05 \times 10^{+8}$	$7.70 \times 10^{+2}$
11	2.66	2.47	2.60	0.19	0.33	0.16	0.42	0.24	$1.01 \times 10^{+8}$	$3.89 \times 10^{+4}$
12	2.65	2.44	2.61	0.21	0.32	2.57	3.00	3.69	$9.87 \times 10^{+7}$	$7.62 \times 10^{+5}$
13	2.60	2.44	2.73	0.16	0.35	0.15	0.81	0.41	$1.02 \times 10^{+8}$	$2.88 \times 10^{+4}$
14	2.67	2.44	2.52	0.23	0.33	0.01	0.14	0.01	$1.02 \times 10^{+8}$	$3.47 \times 10^{+3}$
15	2.57	2.36	2.73	0.21	0.27	0.13	5.38	4.86	$7.81 \times 10^{+7}$	$1.62 \times 10^{+3}$
16	2.54	2.36	2.81	0.18	0.23	0.03	0.45	0.83	$6.49 \times 10^{+7}$	$5.37 \times 10^{+2}$
17	2.54	2.36	2.87	0.18	0.21	0.15	7.59	2.38	$6.00 \times 10^{+7}$	$1.33 \times 10^{+4}$
18	2.46	2.18	2.24	0.28	0.24	0.08	0.05	0.03	$6.38 \times 10^{+7}$	$1.28 \times 10^{+1}$
19	2.57	2.34	2.47	0.22	0.20	0.03	0.30	0.12	$5.72 \times 10^{+7}$	$4.10 \times 10^{+3}$
20	2.59	2.38	2.52	0.21	0.18	0.58	3.82	0.96	$5.08 \times 10^{+7}$	$3.23 \times 10^{+6}$
21	2.53	2.34	2.65	0.20	0.26	0.09	0.43	0.67	$7.32 \times 10^{+7}$	$1.93 \times 10^{+3}$
22	2.56	2.39	2.76	0.17	0.25	0.04	0.90	0.87	$6.99 \times 10^{+7}$	$1.71 \times 10^{+3}$
23	2.56	2.39	2.86	0.18	0.23	0.17	3.79	3.90	$6.44 \times 10^{+7}$	$1.67 \times 10^{+4}$
24	2.50	2.20	2.33	0.31	0.24	0.17	0.19	0.06	$6.58 \times 10^{+7}$	$3.63 \times 10^{+1}$
25	2.58	2.36	2.50	0.22	0.22	0.08	0.32	0.30	$6.29 \times 10^{+7}$	$1.66 \times 10^{+4}$
26	2.58	2.37	2.52	0.21	0.19	0.66	2.23	2.24	$5.64 \times 10^{+7}$	$9.39 \times 10^{+5}$
27	2.59	2.42	2.94	0.17	0.28	0.05	0.65	0.30	$8.20 \times 10^{+7}$	$1.98 \times 10^{+3}$
28	2.57	2.33	2.38	0.25	0.23	0.01	0.19	0.11	$6.71 \times 10^{+7}$	$4.12 \times 10^{+3}$

pivotal for evaluating the TADF effectiveness of the emitters, and the calculated values are listed in Table 1. The S_1 and T_1 energies exhibit opposing trends between the B-N-B and N-B-N frameworks upon modification of the MR-TADF skeleton, chiral unit, or heavy-atom substituents. For example, in the B-N-B framework, both the S_1 and T_1 energies decrease with heavy-atom substitution (O → S → Se) but increase when the chiral unit is altered from type 1 to type 2. This opposing trend is clear from the data: in the series from molecule 1 to 2 to 3, S_1 decreases from 2.57 to 2.44 to 2.44 eV while T_1 decreases from 2.43 to 2.32 to 2.32 eV. Conversely, changing the chiral unit from 1 to 2, as seen in comparing molecules 1 and 4, increases the energies, with S_1 rising from 2.57 to 2.74 eV and T_1 rising from 2.43 to 2.55 eV. In contrast, modifications to the MR-TADF skeleton itself have only a minimal and non-systematic impact. This trend is inverted for the N-B-N framework. Here, heavy-atom substitution slightly increases S_1 and T_1 energies (with S- and Se-containing emitters showing similar values), while changes to the MR-TADF skeleton or chiral unit lower the excited-state energies, which is opposite to their effect observed in B-N-B-based molecules. This clear dichotomy demonstrates that the choice of framework (B-N-B vs. N-B-N) is the dominant factor in determining whether a given structural modification induces a blue or red shift in the excited-state energies. We note that the observed blue or red shift in the S_1 energies, resulting from the four design strategies applied in this study, strongly correlates with changes in the molecular orbital energies and dictates the direction of the S_1 energy shift. For example, within the B-N-B framework, the HOMO energies are destabilized by both heavy-atom substitution and chiral-unit modification, while the MR-TADF skeleton change leads to a slight stabilization (Table S6). Conversely, within the N-B-N framework, the HOMO energies are stabilized only by heavy-atom substitution, while no consistent trend is observed with MR-TADF skeleton or chiral unit changes. This modulation of the HOMO energies directly alters the HOMO-LUMO (H-L) gap: specifically, the gap decreases in the B-N-B framework under the heavy-atom effect and increases in the N-B-N framework under the same effect. Moreover, a strong linear correlation (R^2 = 0.98) between the H-L gap and the S_1 energies confirms that the S_1 electronic configuration is mainly dominated by the HOMO-LUMO transition (Figure 4a). Importantly, the frontier molecular orbital distributions of the HOMO and LUMO, as depicted in Figures S5−S6, reveal a distinct alternating pattern of electron-rich and electron-poor atomic regions, which defines the characteristic MR-TADF nature of these newly designed molecules. The ΔE_{ST} values exhibit systematic trends across the various structural tunings (Table 1). ΔE_{ST} increases from the B-N-B to the N-B-N framework and from chiral unit 1 to chiral unit 2. For instance, for the molecules 1 (B-N-B) and 15 (N-B-N), ΔE_{ST} increased from 0.14 to 0.21 eV, while for molecules 1 (chiral unit 1) and 4 (chiral unit 2), it slightly increased from 0.14 to 0.15 eV. In contrast, ΔE_{ST} decreases with the heavy-atom effect (O → S → Se); this reduction is expected to significantly influence the RISC rate. For example, for molecules 1−3, the ΔE_{ST} values decline from 0.14 to 0.12 to 0.11 eV. A similar trend in the chiral unit change and the

https://doi.org/10.1021/acs.jpcc.6c01502
J. Phys. Chem. C 2026, 130, 7812−7825

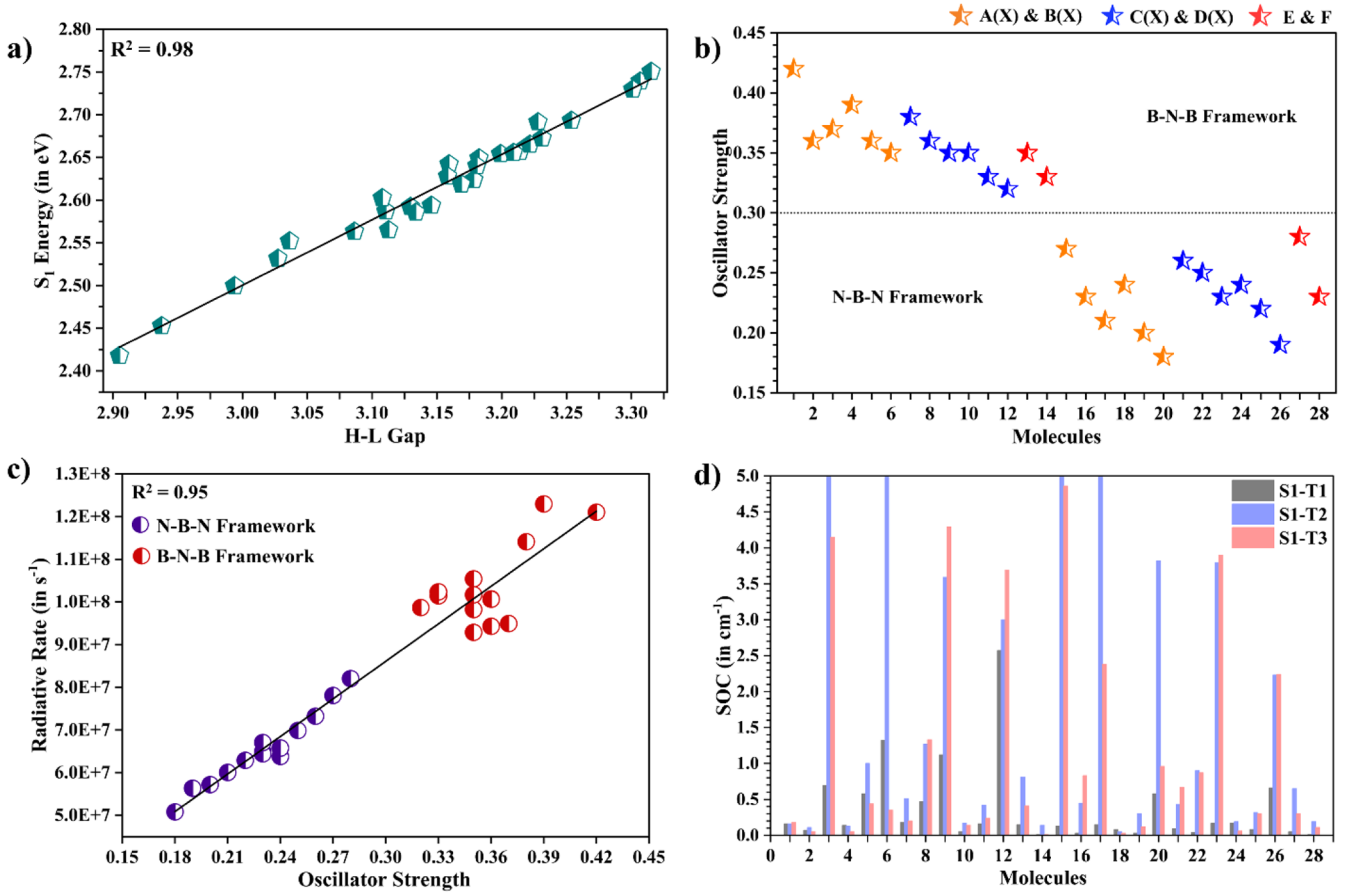

Figure 4. Correlation between H-L gap and S_1 energy (a), calculated oscillator strength (b), correlation between oscillator strength and radiative rate (c), and SOC magnitudes (d).

heavy-atom effect is also observed for the N-B-N framework emitters. Notably, modification of the MR-TADF skeleton has a variable effect: ΔE_{ST} slightly increases from skeleton 1 to 2 and decreases for skeleton 3, with skeleton 2 consistently showing slightly higher values.

The oscillator strength (f) is a critical parameter that influences the radiative decay rate between the S_1 and S_0 states. A higher f typically indicates stronger radiative emission, which is essential for efficient emissive nature. The calculated f and k_r values are presented in Table 1, and their trend is shown in Figure 4b. A very systematic decrease in the f value is observed across all four strategies: from the B-N-B to the N-B-N framework, MR-TADF skeletons 1 to 3, with chiral unit changes from 1 to 2, and under the heavy-atom effect from O to S to Se. This consistent trend indicates that each of these structural strategies plays a significant role in modulating the emitter's radiative rates. More importantly, the framework modulation has a greater impact on the f than other structural tunings. For example, the f values for B-N-B framework emitters range from 0.32 to 0.42, which are significantly higher than those for the N-B-N framework (0.18 to 0.28). They highlight that the initial choice of framework is more critical than other tuning strategies for enhancing the radiative decay in MR-TADF design. This dominant role of the framework is further confirmed by the strong linear correlation ($R^2 = 0.95$) observed between the f and the radiative rate across all emitters (Figure 4c). The calculated SOC magnitudes between the S_1-T_1, S_1-T_2, and S_1-T_3 states are given in Table 1, with trends illustrated in Figure 4d. The SOC magnitudes increase with the atomic weight of the heavy atoms, following the order O < S < Se, for all S_1-T_1, S_1-T_2, and S_1-T_3 states across all molecules. This trend aligns with the well-studied heavy-atom effect, in which increased atomic radius (or atomic number) enhances SOC. This implies that the heavy-atom effect, along with coupling between the higher T_n and S_1 states, enhances spin-vibronic coupling, thereby increasing the overall RISC rate of the systems. Furthermore, emitters based on chiral unit 1 show higher SOC magnitudes than those based on chiral unit 2. For instance, comparing molecules 1 and 4, and molecules 7 and 10, the SOC values decrease from 0.16 to 0.14 cm^{-1} and from 0.18 to 0.05 cm^{-1}, respectively. Unlike chiral unit 2, which contains only carbon and hydrogen, chiral unit 1 has an extra heavy sulfur atom that enhances SOC. More importantly, the B-N-B framework exhibits higher SOC magnitudes than the N-B-N framework. This indicates that SOC depends not only on the heavy-atom effect but also on the molecular framework, primarily because of differences in structural relaxation. The B-N-B emitters exhibit less geometric relaxation, as evidenced by their lower reorganization energy and fewer active vibrational modes, which contribute to their improved SOC magnitudes. Furthermore, variation in SOC magnitudes across the MR-TADF skeletons (1 to 3) appears to be indistinguishable and trendless. Therefore, SOC magnitude analysis in these MR-TADF systems demonstrates that the primary determinants are the inherent molecular framework and the strategic incorporation of heavy atoms, irrespective of their placement in the peripheral cores.

https://doi.org/10.1021/acs.jpcc.6c01502
J. Phys. Chem. C 2026, 130, 7812−7825

Table 2. Calculated Electric (EDM in $\times 10^{-18}$ esu cm), Magnetic (MDM in $\times 10^{-21}$ erg G^{-1}) Dipole Moments, Electric-Magnetic Dipole Moment Angle (E-M in °), Rotatory Strength (10^{-40} erg·esu·cm·G^{-1}), and Dissymmetry Factor g_{lum} (in $\times 10^{-3}$) Values

Molecules	EDM	MDM	E-M	Cos θ	R	g_{lum}
1	6.28	9.88	97.70	−0.13	−86	−0.84
2	5.97	8.31	101.23	−0.19	−100	−1.08
3	5.86	7.39	104.55	−0.25	−113	−1.27
4	5.96	13.33	99.27	−0.16	−132	−1.44
5	5.65	11.08	102.21	−0.21	−138	−1.66
6	5.58	9.38	105.12	−0.26	−141	−1.75
7	6.06	11.17	101.36	−0.20	−137	−1.45
8	5.78	9.32	102.50	−0.22	−120	−1.40
9	5.61	8.48	103.81	−0.24	−117	−1.44
10	5.78	13.68	103.46	−0.23	−189	−2.21
11	5.52	11.70	104.47	−0.25	−167	−2.12
12	5.41	10.37	105.55	−0.27	−155	−2.06
13	5.81	12.75	107.27	−0.30	−225	−2.61
14	5.59	14.08	108.96	−0.32	−261	−3.28
15	4.92	8.11	108.50	−0.32	−133	−2.09
16	4.55	7.82	116.71	−0.45	−166	−3.09
17	4.43	7.68	119.68	−0.50	−175	−3.44
18	4.72	8.96	110.22	−0.35	−153	−2.62
19	4.21	8.70	118.71	−0.48	−184	−3.97
20	4.08	8.25	120.96	−0.51	−180	−4.17
21	4.95	8.60	110.58	−0.35	−156	−2.44
22	4.74	8.76	116.15	−0.44	−189	−3.26
23	4.69	8.69	118.05	−0.47	−198	−3.49
24	4.72	9.41	110.59	−0.35	−163	−2.81
25	4.44	9.69	116.70	−0.45	−201	−3.93
26	4.39	9.42	118.39	−0.48	−204	−4.08
27	5.00	9.80	116.50	−0.45	−226	−3.50
28	4.90	10.72	115.70	−0.43	−228	−3.92
Helicene-BN	4.90	4.70	112.51	−0.38	−92	−1.47

The calculated RISC rates are listed in Table 1. Generally, a lower ΔE_{ST} and higher SOC are strongly associated with a faster RISC process. We have already discussed the systematic trends in ΔE_{ST} and SOC across different modifications in MR-TADF systems. The RISC rates are also strongly correlated with these previously discussed trends. To improve our model, we included contributions from both the $T_1 \rightarrow S_1$ and $T_2 \rightarrow S_1$ channels, where the T_2 state lies below the S_1 state, thereby enabling thermal population via Boltzmann statistics. As shown in Table 1, the RISC rate systematically increases from the N-B-N to the B-N-B framework, from chiral unit 2 to chiral unit 1, and with the heavy-atom effect from O to S to Se. This trend aligns strongly with the corresponding changes in ΔE_{ST} and SOC magnitudes. Notably, molecules based on the B-N-B framework exhibit RISC rates approximately 1 to 3 orders of magnitude higher than those based on the N-B-N framework. Furthermore, selenium-based emitters achieve RISC rates in the range of $\sim 10^{+4}$ to $\sim 10^{+7}$ s^{-1} across both framework-based emitters. Overall, the B-N-B framework demonstrates superior TADF efficiency compared to the N-B-N framework, as evidenced by its favorable FWHM, ΔE_{ST}, SOC, and RISC characteristics. It is also noteworthy that the MR-TADF skeleton 3 maintains consistent color purity and RISC performance across both underlying B-N-B and N-B-N frameworks.

4.3. CPL Properties

We now turn to a discussion of the chiral properties of the systems investigated in this study. In CP-MR-TADF molecules, the EDM, MDM, E-M angle, rotatory strength (R), and g_{lum} are key parameters that provide insights into the overall performance of chiroptical properties, and the calculated values are given in Tables 2 and S7. For achieving a high g_{lum}, which requires a chiral emitter to maximize $|\mu_m|$, and while minimizing $|\mu_e|$, and to align θ such that the two moments are either parallel or antiparallel. The $|\mu_e|$ values systematically decrease under three distinct modifications (Figure 5a): changing the framework from B-N-B to N-B-N, switching from chiral unit 1 to chiral unit 2, and introducing the heavy atom effect from O to S to Se. For example, when the framework changes from B-N-B to N-B-N, the $|\mu_e|$ value decreases from 2.47 to 1.94 a.u. (comparing molecule 1 and 15) and from 2.35 to 1.79 a.u. (similarly comparing molecule 2 and 16). When chiral unit 1 is replaced with chiral unit 2, the value decreases from 2.47 to 2.34 a.u. (molecules 1 and 4) and from 1.94 to 1.86 a.u. (molecules 15 and 18). Introducing heavier atoms also leads to a systematic decrease: values fall from 2.47 to 2.35 to 2.31 a.u. (molecules from 1 to 3) and from 1.94 to 1.79 to 1.74 a.u. (molecules from 14 to 16) when shifting from O to S to Se, respectively. An analysis of the MR-TADF skeleton shift shows that the $|\mu_e|$ value decreases systematically within the B-N-B framework, while in the N-B-N framework, it shows a slight increase or remains relatively unchanged. An analysis of the $|\mu_m|$ reveals a similar trend to the $|\mu_e|$ for framework changes and heavy atom effects, but opposite trends for chiral unit and MR-TADF skeleton modifications (Figure 5b). For framework changes from B-

https://doi.org/10.1021/acs.jpcc.6c01502
J. Phys. Chem. C 2026, 130, 7812−7825

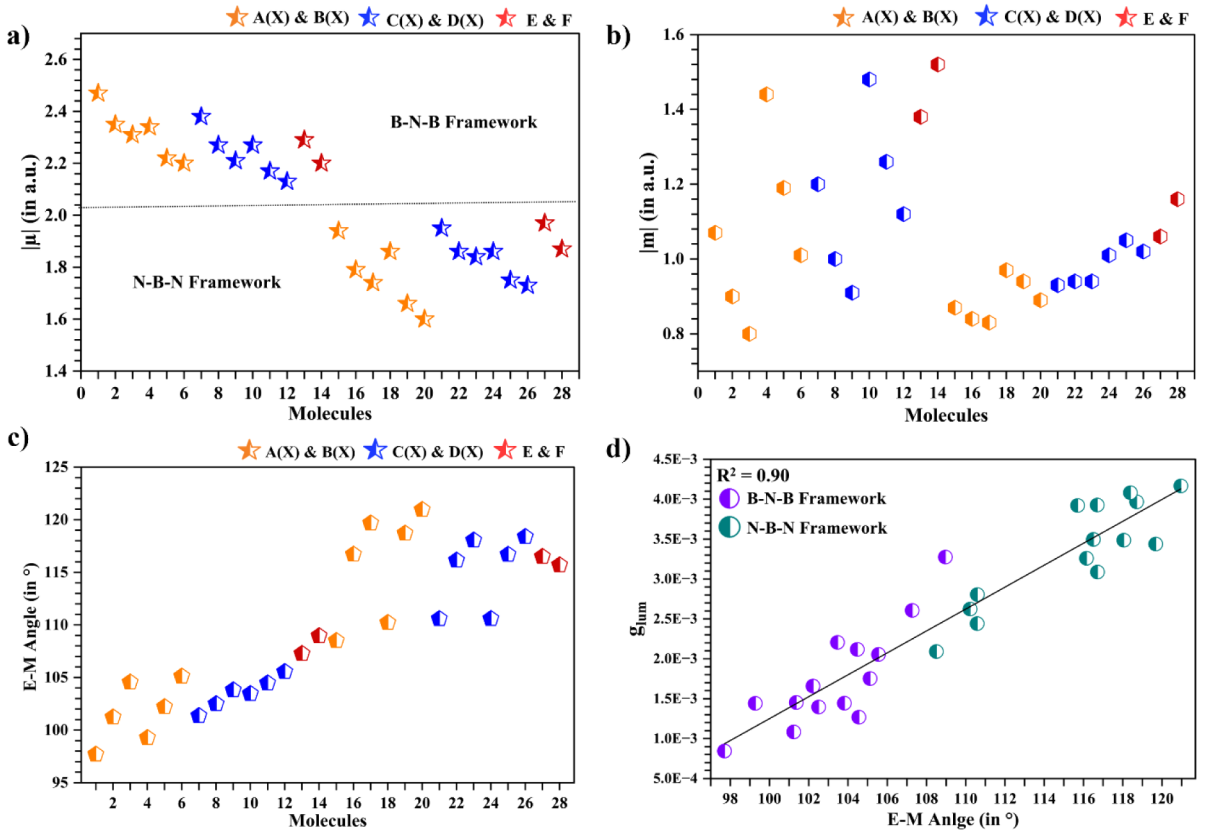

Figure 5. Transition electric (a), magnetic (b) dipole moments, respectively, E-M angle (c), and correlation between g_{lum} and E-M angle (d).

N-B to N-B-N, the $|\mu_m|$ value decreases from 1.07 to 0.87 a.u. (molecule 1 vs. 15) and from 0.90 to 0.84 a.u. (molecule 2 vs. 16). The heavy atom effect also causes a decrease, with values falling from 1.07 to 0.90 to 0.80 a.u. (molecules 1 to 3) and from 0.87 to 0.84 to 0.83 a.u. (molecules 14 to 16). In contrast, changes to the chiral unit and the MR-TADF skeleton increase $|\mu_m|$ values, the opposite of their effect on $|\mu_e|$. For instance, replacing chiral unit 1 with chiral unit 2 increases the $|\mu_m|$ from 1.07 to 1.44 a.u. (molecules 1 and 4) and from 0.87 to 0.97 a.u. (molecules 15 and 18). Similarly, altering the MR-TADF skeleton from 1 to 3 raises the value from 1.07 to 1.20 to 1.38 a.u. for molecules 1, 7, and 13, and from 0.87 to 0.93 to 1.06 a.u. for molecules 15, 21, and 27. The structural origins of the $|\mu_e|$ and $|\mu_m|$ are further investigated hereinafter. We conduct a decomposition analysis of the transition electric and magnetic dipole moment densities and obtain the atomic contributions to investigate the relationship between molecular structures and chiroptical properties. To analyze the effect of the framework shift, molecules 1 and 15 were investigated first. As shown in Figure 6 and Table S7, the net electric and magnetic dipole moment density along the Y-axis is zero because the equal densities in the positive and negative regions or directions cancel each other out. When the framework shifts from B-N-B to N-B-N, the μ_e value along the X-axis decreases from −2.42 to −1.94 a.u. Specifically, carbon atoms 22 and 23, which are connected to both nitrogen atoms in molecule 15, exhibit opposing electric vectors (positive parts) with significant magnitudes, each contributing approximately 0.18 a.u., thereby lowering the value along the X-axis. In contrast, the corresponding atoms connected to both boron atoms in molecule 1 show negligible values in the negative parts. Similarly, the reduction in the μ_m from −1.01 to −0.82 a.u. along the Z-axis between molecules 1 and 15 is primarily due to contributions from carbon atoms 7, 13, and 16. Specifically, carbon atom 7 shows an increase in its positive (opposing) vector from 0.08 to 0.15 a.u., while the negative vector magnitudes for carbons 13 and 16 are significantly reduced from −0.18 to −0.06 a.u., respectively. Furthermore, shifting the MR-TADF skeleton from molecules 1 to 7 to 13 shows a correlation where the positive/negative vector ratio increases with the μ_e and indicates that contributions opposing the dominant direction play a key role in reducing the net μ_e value along the X-axis (Figure S7). Conversely, along the Z-axis, this ratio slightly decreases with the μ_m, correlating with the observed increase in μ_m across this series. A similar trend is observed for the chiral unit change between molecules 1 and 4, as shown in Figure S8. Additionally, the heavy atom effect (O → S → Se) decreases both the μ_e and μ_m along the X- and Z-axis, respectively (Figure S9). For both the electric and magnetic vectors, the magnitude of the positive-direction vector increases while the negative vector decreases, leading to a significant increase in the positive/negative ratio. However, a closer analysis of the μ_e reveals that while the negative vector on the heavy atom (O, S, Se) itself increases, there is a compensatory decrease in the contributions of neighboring carbon atoms. This opposing effect nullifies the overall heavy atom influence on the net $|\mu_e|$ value. The above mentioned analyses of dipole moment density and atomic vector projections revealed that molecular engineering strategies, including manipulation of the lone pair electron on nitrogen and the empty orbital of boron within the B-N-B and N-B-N frameworks, the architecture of the MR-TADF skeleton from X to non-X sites, the chiral unit composition (with heavy atoms or with C/H), and the heavy atom effect from O to S to

https://doi.org/10.1021/acs.jpcc.6c01502
J. Phys. Chem. C 2026, 130, 7812−7825

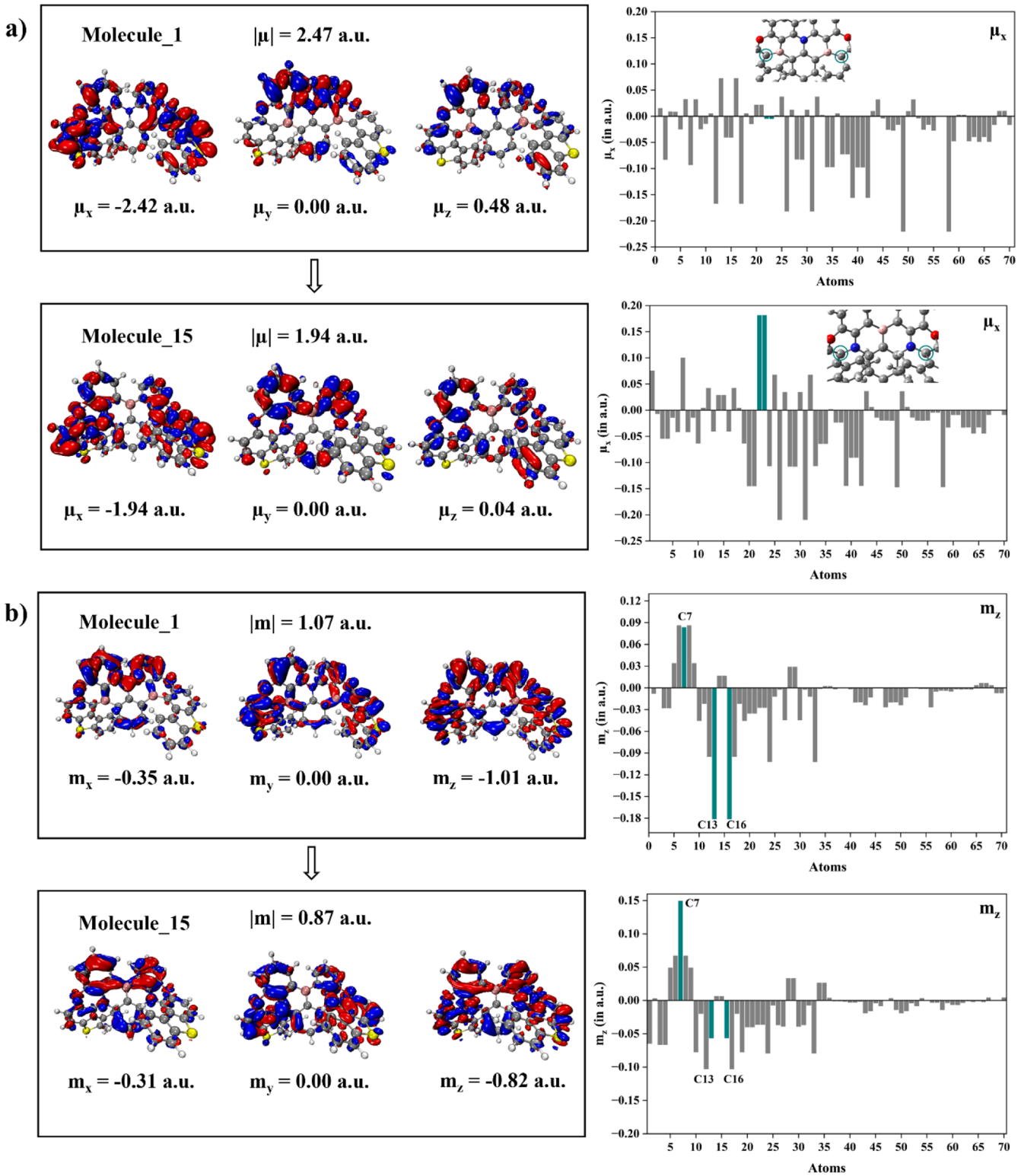

Figure 6. Comparison of the molecular frameworks of 1 (B-N-B) and 15 (N-B-N), showing (a) electric and (b) magnetic dipole moment densities (isovalue = 0.002), with atomic contribution vectors. Blue and red represent positive and negative parts, respectively.

Se, all significantly affect the electric and magnetic dipole moment vectors through modulation of nearby carbon atom environments. Interestingly, the structural evolution toward a carbon-rich environment in the molecular structures promotes the $|\mu_m|$ while simultaneously reducing the $|\mu_e|$ within both the B-N-B and N-B-N frameworks. Furthermore, strategic molecular design, specifically the choice of chiral unit and the MR-TADF scaffold architecture, emerges as the principal route for amplifying the $|\mu_m|$ in these systems, whereas the heavy atom effect tends to diminish it.

The E-M angle increases with changes to the frameworks, MR-TADF skeletons, chiral units, and heavy atom effects. Changes in MR-TADF skeletons, chiral units, and heavy atom effects typically amplify the angle by approximately 1° to 5°

https://doi.org/10.1021/acs.jpcc.6c01502
J. Phys. Chem. C 2026, 130, 7812−7825

(Table 2 and Figure 5c), whereas framework modifications have a significantly greater impact, increasing it by about 10° to 15°. For example, when the chiral unit changes from chiral unit 1 to chiral unit 2, the E-M angle increases slightly from 98° to 99° (molecules 1 and 4). The heavy atom effect produces a more pronounced change, increasing the angle from 98° to 101° to 105° (molecules from 1 to 2 to 3). Similarly, changes in the MR-TADF skeleton increase the angle from 98° to 101° to 107° (molecules 1, 7, and 13). However, switching from B-N-B to N-B-N significantly shifts the angle toward an anti-parallel orientation compared to B-N-B. For instance, the angle increases from 98° to 109° (molecules 1 and 15) and from 101° to 117° (molecules 2 to 16). Therefore, the E-M angle is dominated primarily by the framework, followed by the heavy atom effect and MR-TADF skeleton changes, whereas chiral unit modifications have a very minimal effect.

Rotatory strength (R), which quantifies a molecule's ability to rotate plane-polarized light, generally correlates with stronger CPL signals when higher. The R values systematically increase with changes in the framework, the MR-TADF skeleton, the chiral unit, and the heavy-atom effects (Table 2). The calculated ECD spectra of all newly designed molecules display symmetry about the X-axis. This spectral signature confirms the manifestation of a cotton effect and, consequently, the efficacy of the intrinsic chiral perturbation strategy (Figures S10−S11). For example, when the framework changes from B-N-B to N-B-N, R increases from 86 to 133 (comparing molecules 1 and 15) and from 100 to 166 (comparing molecules 2 and 16). Changes in the MR-TADF skeletons from 1 to 2 to 3 also lead to significant increases: from 86 to 137 to 225 for molecules 1, 7, and 13, and from 133 to 156 to 226 for molecules 15, 21, and 23. Similarly, replacing chiral unit 1 with chiral unit 2 raises R from 86 to 132 (molecules 1 and 4) and from 100 to 138 (molecules 2 and 5). In contrast, the heavy atom effect generally leads to a systematic increase in R values, though exceptions exist, such as in the series from molecule 7 to 12, where R slightly decreases. Therefore, the MR-TADF skeleton, the framework, and the chiral unit serve as powerful levers for increasing R, whereas the heavy-atom effect has a comparatively lesser impact.

The g_{lum} values follow a systematic trend across all four structural modifications (Table 2). For instance, changing the framework from B-N-B to N-B-N increases g_{lum} from 8.44E-04 to 2.09E-03 for molecules 1 and 15, and from 1.08E-03 to 3.09E-03 for molecules 2 and 16. Similarly, modifying the MR-TADF skeleton from type 1 to 2 to 3 increases g_{lum} from 8.44E-04 to 1.45E-03 to 2.61E-03 across molecules 1, 7, and 13, and from 2.09E-03 to 2.44E-03 to 3.50E-03 across molecules 15, 21, and 23. Replacing chiral unit 1 with chiral unit 2 also increases g_{lum}, as seen in the increase from 8.44E-04 to 1.44E-03 for molecules 1 and 4, and from 1.08E-03 to 1.66E-03 for molecules 2 and 5. While the heavy atom effect generally produces a systematic increase in g_{lum}, for example, from 8.44E-04 to 1.08E-03 to 1.27E-03 across molecules 1 to 3, exceptions exist, such as the slight decrease observed across the series from molecule 7 to 12. The g_{lum} value shows a strong correlation with both the E-M angle and the EDM, as evidenced by correlation diagrams with R^2 values of approximately 0.90 (Figure 5d) and 0.77 (Figure S12), respectively. These results indicate that higher g_{lum} values are achieved under conditions where the E-M angle is maximized, and the EDM is minimized. Notably, molecules 16 (with chiral unit 1) and 19 (with chiral unit 2), designed through extended helicene modification, exhibited significantly increased CPL intensity, yielding g_{lum} values of 3.09E-03 and 3.97E-03, respectively, which are substantially higher than the experimentally reported Helicene-BN emitter (g_{lum} = 1.47E-03). This improvement is due to the favorable progression from Helicene-BN to molecules 16 (extended helicene with chiral unit 1) to 19 (extended helicene with chiral unit 2), characterized by a decreased EDM, an increased MDM, and a larger E-M angle. Based on the analysis of CPL properties, the following key observations guide the design direction toward achieving high g_{lum} values: (i) EDM values decrease across all four design strategies, (ii) MDM values increase with all strategies except the heavy atom effect, which reduces them, (iii) the E-M angle increases with all structural tunings, while the heavy atom effect exerts only a slight influence, (iv) the g_{lum} values increase under all strategies except the heavy atom effect in certain cases, notably for molecules 7−12.

4.4. Racemization of CP-MR-TADF Emitters

Racemization, the process by which a chiral molecule converts from one conformer to another, is a critical factor in the design and performance of CP-MR-TADF emitters. The stability of the chiral configuration against racemization is essential for maintaining the desired CPL properties.[47] The calculated racemization barriers (RB), intermediate energies, and racemization process are listed and shown in Table S8 and Figure 7. Structural modifications significantly influence the racemization energies. To analyze the framework effect, we compared molecules 4 and 18, 10 and 24, and 14 and 28 (Figure S13). Changing the framework from B-N-B to N-B-N substantially increases RB from 24.29 to 40.67, 23.97 to 41.01, and 22.24 to 40.77 kcal mol^{-1}, respectively. Within the B-N-B framework, the MR-TADF skeleton has a minor influence: for molecules 4, 10, and 14, RB decreases only slightly from 24.29 to 23.97 to 22.24 kcal mol^{-1} (Figure S13). In the N-B-N framework (molecules 18, 24, and 28), RB remains consistently near ∼40 kcal mol^{-1}, showing negligible variation (Figure 8a). Chiral unit modification also has a minimal effect, as seen in the slight decrease from 41.98 to 40.67 kcal mol^{-1}

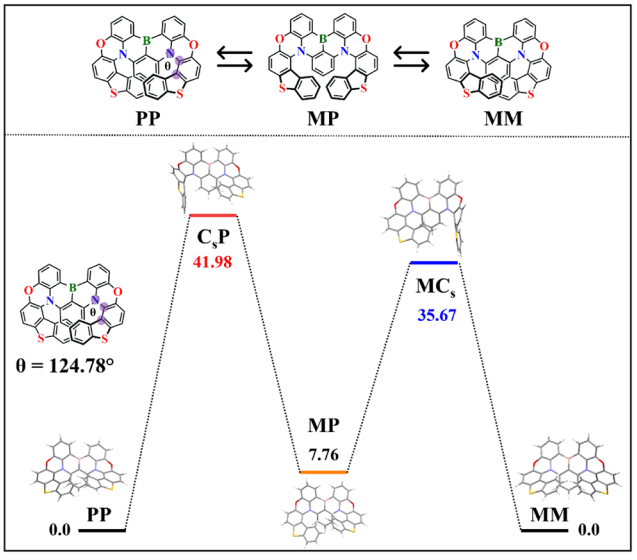

Figure 7. The racemization process between PP and MM conformers for molecule 15 and the relative free energy in kcal mol^{-1}.

https://doi.org/10.1021/acs.jpcc.6c01502
J. Phys. Chem. C 2026, 130, 7812−7825

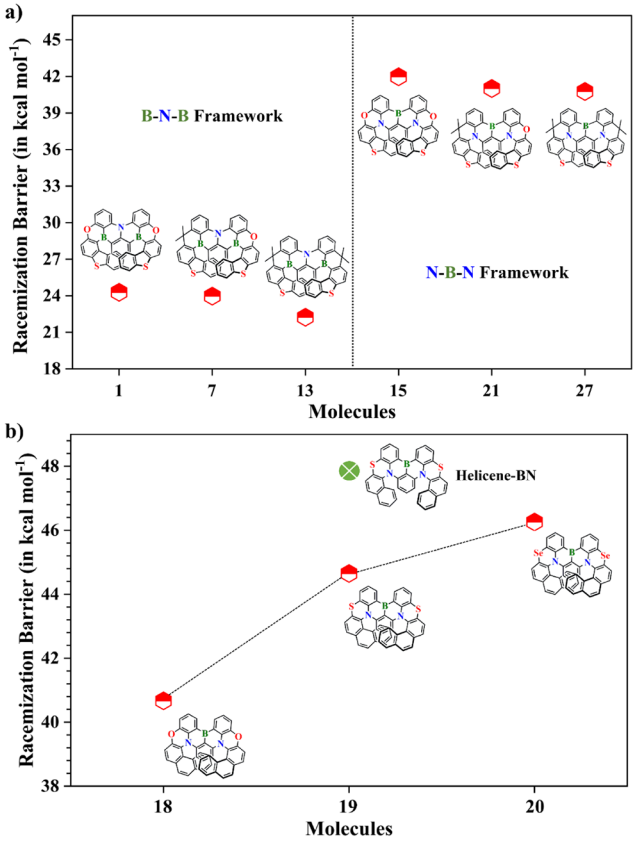

Figure 8. Comparison of racemization barriers across different molecular frameworks B-N-B vs. N-B-N (a), the heavy atom effect (b), and the relative free energies in kcal mol^{-1}.

for molecules 15 (chiral unit 1) and 18 (chiral unit 2) (Figure S14). In contrast, the heavy-atom effect systematically increases RB, as demonstrated by the progression from 40.67 to 44.65 to 46.25 kcal mol^{-1} for molecules 18, 19, and 20 (Figures 8b and S15). Overall, the framework (B-N-B vs. N-B-N) plays the dominant role, with the N-B-N framework increasing the barrier by ∼20 kcal mol^{-1} relative to the B-N-B framework (Figure 8a). This difference arises from framework-specific helicity that imposes distinct steric constraints on the helical unit. In the B-N-B framework, the larger B-C-C bond angle (>124°) creates greater spatial freedom, allowing the helicene subunit to rotate more freely. Conversely, in the N-B-N framework, the smaller N-C-C angle (<124°) brings the helicene unit closer to the MR-TADF core, thereby restricting its conformational mobility. The resulting steric hindrance raises the rotational energy barrier, as evidenced by the higher computed values in the N-B-N systems. The heavy atom effect slightly elevates RB in the order O < S < Se, while chiral unit and MR-TADF skeleton modifications have a negligible impact. Notably, the experimentally reported Helicene-BN CPL emitter with five helicene rings exhibits an RB of 47.82 kcal mol^{-1}, which is only 3.17 kcal mol^{-1} higher than that of its extended six-helicene analogue, molecule 19 (44.65 kcal mol^{-1}) (Figure 8b). This relatively small increase in barrier can be rationalized by the fact that the N-C-C bond angle in the Helicene-BN system is slightly smaller (∼120.99°) than that in molecule 19 (N-C-C = 121.75°). This structural similarity is further supported by comparison with the Se-substituted analogue, molecule 20, which exhibits a comparable barrier (46.26 kcal mol^{-1}) and a nearly identical N-C-C angle (∼120.98°).

5. CONCLUSIONS

In summary, this study primarily aimed to optimize organic MR-TADF emitters toward high g_{lum} by leveraging frameworks, MR-TADF skeletons, chiral units, and heavy-atom-effect structural modifications. To accurately predict the photophysical properties of CP-MR-TADF emitters, a detailed benchmark study was conducted to identify the most reliable methods among well-established ones. The benchmark study revealed that the STEOM-DLPNO-CCSD method demonstrated superior accuracy in predicting the excited-state properties of CP-MR-TADF emitters. Molecules based on the B-N-B framework exhibit improved color purity, with FWHM values ranging from ∼14 to ∼18 nm, a result of their lesser structural relaxation, while those based on the N-B-N framework show broader emission, with FWHM values between ∼18 and ∼36 nm. Notably, the FWHM of MR-TADF skeleton 3-based molecules is unaffected by the choice of framework, as all four molecules 13, 14, 27, and 28 yield consistently narrow FWHM values within the ∼17−18 nm range. These results underscore the importance of both framework selection and MR-TADF architecture in controlling color purity. The RISC rates for S- and Se-integrated molecules, including MR-TADF skeleton 3-based molecules (13, 14, 27, and 28), fall within the range of $\sim10^3$ to 10^7 s^{-1}. This enhanced rate is attributed to their increased SOC magnitude and small ΔE_{ST} gaps. All molecules exhibit g_{lum} values on the order of $\sim10^{-3}$. Comparatively, the N-B-N framework yields higher g_{lum} values than the B-N-B framework, a result attributable to its larger E-M angles and the smaller EDM values. Similarly, in both frameworks, all structural modifications increased the g_{lum} values toward higher magnitudes, a trend pronounced in carbon-rich environments, although the heavy-atom effect specifically failed to improve the magnetic vectors. Thus, Skeleton 3 exhibits framework- and chiral unit-independent behavior, reliably affording a narrow emission bandwidth and high g_{lum} as well. This comprehensive theoretical investigation deepens the understanding of the structure-property relationship toward achieving desired photophysical and chiroptical properties in CP-MR-TADF emitters. By evaluating synergistic structural modifications, including the framework (B-N-B vs. N-B-N), the MR-TADF skeleton architecture, chiral units, and the heavy-atom effect, this work offers a rational design strategy to enhance g_{lum}.

■ ASSOCIATED CONTENT

Supporting Information

The Supporting Information is available free of charge at https://pubs.acs.org/doi/10.1021/acs.jpcc.6c01502.

Benchmark studies; FWHM; reorganization energies; HR factors; HOMO-LUMO energies and their distributions; electric-magnetic dipole moment vectors; densities of electric-magnetic dipole moments; atom's contribution to electric-magnetic dipole moments; racemization barrier energies and their process (PDF)

https://doi.org/10.1021/acs.jpcc.6c01502
J. Phys. Chem. C 2026, 130, 7812−7825

AUTHOR INFORMATION

Corresponding Author

Zhigang Shuai − *Guangdong Basic Research Center of Excellence for Aggregate Science, School of Science and Engineering, The Chinese University of Hong Kong, Shenzhen, Guangdong 518172, P. R. China; MOE Key Laboratory of Organic OptoElectronics and Molecular Engineering, Department of Chemistry, Tsinghua University, Beijing 100084, China;* orcid.org/0000-0003-3867-2331; Email: shuaizhigang@cuhk.edu.cn

Authors

Ramalingam Mahaan − *Guangdong Basic Research Center of Excellence for Aggregate Science, School of Science and Engineering, The Chinese University of Hong Kong, Shenzhen, Guangdong 518172, P. R. China;* orcid.org/0000-0002-7722-3515

Weitang Li − *Guangdong Basic Research Center of Excellence for Aggregate Science, School of Science and Engineering, The Chinese University of Hong Kong, Shenzhen, Guangdong 518172, P. R. China;* orcid.org/0000-0002-8739-641X

Complete contact information is available at: https://pubs.acs.org/10.1021/acs.jpcc.6c01502

Notes

The authors declare no competing financial interest.

ACKNOWLEDGMENTS

This work was supported by the National Natural Science Foundation of China (grant nos. 22433007 and T2350009), the Guangdong Basic Research Center of Excellence for Aggregate Science, the Guangdong Provincial Natural Science Foundation (grant no. 2024A1515011185), and the Shenzhen City Peacock Team Project (grant no. KQTD20240729102028011). The computing exercise in this work was conducted on the High-Performance Computing Portal, which is under the administration of the Information Technology Services Office (ITSO) at the Chinese University of Hong Kong, Shenzhen.

REFERENCES

(1) Guido, C. A.; Zinna, F.; Pescitelli, G. Quantum Chemistry Calculations of Circularly Polarized Luminescence (CPL): From Spectral Modeling to Molecular Design. *Chem. Rev* **2025**, *125* (21), 10492−10656.

(2) Furlan, F.; Moreno-Naranjo, J. M.; Gasparini, N.; Feldmann, S.; Wade, J.; Fuchter, M. J. Chiral Materials and Mechanisms for Circularly Polarized Light-Emitting Diodes. *Nat. Photonics* **2024**, *18* (7), 658−668.

(3) Jiang, H.; Ai, D.; Jin, J.; Xie, Z.; Wong, W.-Y. Recent Progress in Circularly Polarized Multi-Resonance Thermally Activated Delayed Fluorescence Materials for Organic Light-Emitting Diodes. *Sci. China: Chem* **2025**, *68* (7), 2804−2819.

(4) Zhong, Y.; Wu, Z.; Zhang, Y.; Dong, B.; Bai, X. Circularly Polarized Luminescence of Lanthanide Complexes: From Isolated Individuals, Discrete Oligomers, to Hierarchical Assemblies. *InfoMat* **2023**, *5* (3), No. e12392.

(5) Lunkley, J. L.; Shirotani, D.; Yamanari, K.; Kaizaki, S.; Muller, G. Extraordinary Circularly Polarized Luminescence Activity Exhibited by Cesium Tetrakis(3-Heptafluoro-Butylryl-(+)-Camphorato) Eu-(III) Complexes in EtOH and $CHCl_3$ Solutions. *J. Am. Chem. Soc* **2008**, *130* (42), 13814−13815.

(6) Yang, X.; Gao, X.; Zheng, Y.-X.; Kuang, H.; Chen, C.-F.; Liu, M.; Duan, P.; Tang, Z. Recent Progress of Circularly Polarized Luminescence Materials from Chinese Perspectives. *CCS Chem* **2023**, *5* (12), 2760−2789.

(7) Wang, M.; Wang, Z.; Liu, L.; Tian, W. Organic Circularly Polarized Luminescence Materials in Various Aggregation States. *J. Mater. Chem. C Mater* **2025**, *13* (41), 20880−20920.

(8) Li, X.; Xie, Y.; Li, Z. The Progress of Circularly Polarized Luminescence in Chiral Purely Organic Materials. *Adv. Photonics Res* **2021**, *2* (4), 2000136.

(9) Tang, C. W.; Vanslyke, S. A. Organic Electroluminescent Diodes. *Appl. Phys. Lett* **1987**, *51* (12), 913−915.

(10) Adachi, C.; Baldo, M. A.; Forrest, S. R.; Lamansky, S.; Thompson, M. E.; Kwong, R. C. High-Efficiency Red Electrophosphorescence Devices. *Appl. Phys. Lett* **2001**, *78* (11), 1622−1624.

(11) Uoyama, H.; Goushi, K.; Shizu, K.; Nomura, H.; Adachi, C. Highly Efficient Organic Light-Emitting Diodes from Delayed Fluorescence. *Nature* **2012**, *492* (7428), 234−238.

(12) Dos Santos, J. M.; Hall, D.; Basumatary, B.; Bryden, M.; Chen, D.; Choudhary, P.; Comerford, T.; Crovini, E.; Danos, A.; De, J.; et al. The Golden Age of Thermally Activated Delayed Fluorescence Materials: Design and Exploitation. *Chem. Rev* **2024**, *124* (24), 13736−14110.

(13) Liu, M.; Li, C.; Duan, L.; Zhang, D. Recent Advances in Blue Multiple-Resonance Thermally Activated Delayed Fluorescence Materials and Their Applications in Organic Light-Emitting Diodes. *Adv. Opt. Mater* **2026**, *14* (1), No. e03140.

(14) Wu, X.; Ni, S.; Wang, C.-H.; Zhu, W.; Chou, P.-T. Comprehensive Review on the Structural Diversity and Versatility of Multi-Resonance Fluorescence Emitters: Advance, Challenges, and Prospects toward OLEDs. *Chem. Rev* **2025**, *125* (14), 6685−6752.

(15) Wang, J.; Chen, D.; Moreno-Naranjo, J. M.; Zinna, F.; Frédéric, L.; Cordes, D. B.; McKay, A. P.; Fuchter, M. J.; Zhang, X.; Zysman-Colman, E. Helically Chiral Multiresonant Thermally Activated Delayed Fluorescent Emitters and Their Use in Hyperfluorescent Organic Light-Emitting Diodes. *Chem. Sci* **2024**, *15* (41), 16917−16927.

(16) Chen, L.; Zou, P.; Chen, J.; Xu, L.; Tang, B. Z.; Zhao, Z. Hyperfluorescence Circularly Polarized OLEDs Consisting of Chiral TADF Sensitizers and Achiral Multi-Resonance Emitters. *Nat. Commun* **2025**, *16* (1), 1656.

(17) Xu, Y.; Liu, F.; Jiang, Y.; Su, Z.; Ma, X.; Hu, Y.; Lu, P. Circularly Polarized MR-TADF Emitters with an Asymmetric Spiro-Carbon-Locking Architecture for Concentration-Quenching-Resistant Narrowband Circularly Polarized Electroluminescence. *Angew. Chem. Int. Ed* **2026**, *65*, No. e22906.

(18) Bella, G.; Bruno, G.; Santoro, A. Computationally Guided Circularly Polarized Luminescence Simulations in Chiral Adaptive Supramolecular Systems. *J. Mater. Chem. C Mater* **2024**, *12* (44), 17913−17924.

(19) Liu, S.; Liu, S.; Gao, Y.; Lin, L.; Wang, C.-K.; Fan, J.; Song, Y. Modulation of Luminescence Properties of Circularly Polarized Thermally Activated Delayed Fluorescence Molecules with Axial Chirality by Donor Engineering. *Phys. Chem. Chem. Phys* **2024**, *26* (13), 9931−9939.

(20) Wu, X.; Huang, J.; Su, B.; Wang, S.; Yuan, L.; Zheng, W.; Zhang, H.; Zheng, Y.; Zhu, W.; Chou, P. Fabrication of Circularly Polarized MR-TADF Emitters with Asymmetrical Peripheral-Lock Enhancing Helical B/N-Doped Nanographenes. *Adv. Mater* **2022**, *34* (1), 2105080.

(21) Yang, W.; Li, N.; Miao, J.; Zhan, L.; Gong, S.; Huang, Z.; Yang, C. Simple Double Hetero[5]Helicenes Realize Highly Efficient and Narrowband Circularly Polarized Organic Light-Emitting Diodes. *CCS Chem* **2022**, *4* (11), 3463−3471.

(22) Zhang, F.; Rauch, F.; Swain, A.; Marder, T. B.; Ravat, P. Efficient Narrowband Circularly Polarized Light Emitters Based on 1,4-B,N-embedded Rigid Donor−Acceptor Helicenes. *Angew. Chem. Int. Ed* **2023**, *62* (16), No. e202218965.

(23) Ye, Z.; Wu, H.; Xu, Y.; Hua, T.; Chen, G.; Chen, Z.; Yin, X.; Huang, M.; Xu, K.; Song, X.; et al. Deep-Blue Narrowband Hetero[6]Helicenes Showing Circularly Polarized Thermally Acti-

vated Delayed Fluorescence Toward High-Performance OLEDs. *Adv. Mater* **2024**, *36* (1), 2308314.
(24) Pratik, S. M.; McBride, E. P.; Brédas, J.; Coropceanu, V. The Role of Chalcogen Substitution and Helical Frameworks in Designing Efficient Chiral Multi-Resonant TADF Emitters. *Adv. Opt. Mater* **2025**, *13* (23), 2403421.
(25) Jiang, P.; Zhan, L.; Cao, X.; Lv, X.; Gong, S.; Chen, Z.; Zhou, C.; Huang, Z.; Ni, F.; Zou, Y.; et al. Simple Acridan-Based Multi-Resonance Structures Enable Highly Efficient Narrowband Green TADF Electroluminescence. *Adv. Opt. Mater.* **2021**, *9*, 2100825.
(26) Hu, Y. X.; Miao, J.; Hua, T.; Huang, Z.; Qi, Y.; Zou, Y.; Qiu, Y.; Xia, H.; Liu, H.; Cao, X.; et al. Efficient Selenium-Integrated TADF OLEDs with Reduced Roll-Off. *Nat. Photonics* **2022**, *16* (11), 803−810.
(27) Nathiya, S.; Panneerselvam, M.; Costa, L. T. A Theoretical Investigation of Heavy Atom and Oxidation Effects in MR-TADF Emitters for OLEDs: A Combined DFT, Double Hybrid DFT, CCSD, and QM/MM Approaches. *Phys. Chem. Chem. Phys* **2025**, *27* (14), 7265−7278.
(28) Mahaan, R.; John Bosco, A. Sulfur Oxidation State and Substituents Influenced Multifunctional Organic Luminophores in BTP Core for OLEDs: A Computational Study on RTP, TADF Emitter and Sensitizer. *J. Phys. Chem. A* **2023**, *127* (50), 10570−10582.
(29) Mahaan, R.; John Bosco, A. Does BODIPY Drive the "Hot-Exciton" TADF Mechanism? A Detailed Computational Study. *J. Phys. Chem. C* **2024**, *128* (33), 14085−14099.
(30) Pratik, S. M.; Coropceanu, V.; Brédas, J.-L. Purely Organic Emitters for Multiresonant Thermally Activated Delay Fluorescence: Design of Highly Efficient Sulfur and Selenium Derivatives. *ACS Mater. Lett* **2022**, *4* (3), 440−447.
(31) Pratik, S. M.; Coropceanu, V.; Brédas, J.-L. Enhancement of Thermally Activated Delayed Fluorescence (TADF) in Multi-Resonant Emitters via Control of Chalcogen Atom Embedding. *Chem. Mater* **2022**, *34* (17), 8022−8030.
(32) Sanyam; Khatua, R.; Mondal, A. Cost-Effective Approach for Modeling of Multiresonant Thermally Activated Delayed Fluorescence Emitters. *J. Chem. Theory Comput* **2023**, *19* (24), 9290−9301.
(33) Shuai, Z. Thermal Vibration Correlation Function Formalism for Molecular Excited State Decay Rates. *Chin. J. Chem* **2020**, *38* (11), 1223−1232.
(34) McCumber, D. E. Einstein Relations Connecting Broadband Emission and Absorption Spectra. *Phys. Rev* **1964**, *136* (4A), A954−A957.
(35) Marcus, R. A. On the Theory of Electron-Transfer Reactions. VI. Unified Treatment for Homogeneous and Electrode Reactions. *J. Chem. Phys* **1965**, *43* (2), 679−701.
(36) Marcus, R. A. Electron Transfer Reactions in Chemistry. Theory and Experiment. *Rev. Mod. Phys* **1993**, *65* (3), 599−610.
(37) Cho, E.; Liu, L.; Coropceanu, V.; Brédas, J.-L. Impact of Secondary Donor Units on the Excited-State Properties and Thermally Activated Delayed Fluorescence (TADF) Efficiency of Pentacarbazole-Benzonitrile Emitters. *J. Chem. Phys* **2020**, *153* (14), 144708.
(38) Hall, D.; Sancho-García, J. C.; Pershin, A.; Beljonne, D.; Zysman-Colman, E.; Olivier, Y. Benchmarking DFT Functionals for Excited-State Calculations of Donor−Acceptor TADF Emitters: Insights on the Key Parameters Determining Reverse Inter-System Crossing. *J. Phys. Chem. A* **2023**, *127* (21), 4743−4757.
(39) Niu, Y.; Li, W.; Peng, Q.; Geng, H.; Yi, Y.; Wang, L.; Nan, G.; Wang, D.; Shuai, Z. MOlecular MAterials Property Prediction Package (MOMAP) 1.0: A Software Package for Predicting the Luminescent Properties and Mobility of Organic Functional Materials. *Mol. Phys* **2018**, *116* (7−8), 1078−1090.
(40) Niu, Y.; Peng, Q.; Shuai, Z. Promoting-Mode Free Formalism for Excited State Radiationless Decay Process with Duschinsky Rotation Effect. *Sci. China B Chem* **2008**, *51* (12), 1153−1158.
(41) Peng, Q.; Yi, Y.; Shuai, Z.; Shao, J. Toward Quantitative Prediction of Molecular Fluorescence Quantum Efficiency: Role of Duschinsky Rotation. *J. Am. Chem. Soc* **2007**, *129* (30), 9333−9339.
(42) Lu, T.; Chen, F. Multiwfn: A Multifunctional Wavefunction Analyzer. *J. Comput. Chem* **2012**, *33* (5), 580−592.
(43) Linder, M.; Brinck, T. On the method-dependence of transition state asynchronicity in Diels−Alder reactions. *Phys. Chem. Chem. Phys* **2013**, *15* (14), 5108−5114.
(44) Frisch, M. J.; Trucks, G. W.; Schlegel, H. B.; Scuseria, G. E.; Robb, M. A.; Cheeseman, J. R.; Scalmani, G.; Barone, V.; Petersson, G. A.; Nakatsuji, H., et al., *Gaussian 16, Revision C.01*, Gaussian, Inc., 2016.
(45) Neese, F. The ORCA Program System. *WIREs Comput. Mol. Sci* **2012**, *2* (1), 73−78.
(46) Chen, Z.; Guo, W.-C.; Chen, C.-F. Recent Advances in the Synthesis of Multiple Helicenes. *Org. Biomol. Chem* **2025**, *23* (33), 7501−7520.
(47) Barroso, J.; Cabellos, J. L.; Pan, S.; Murillo, F.; Zarate, X.; Fernandez-Herrera, M. A.; Merino, G. Revisiting the Racemization Mechanism of Helicenes. *Chem. Commun* **2018**, *54* (2), 188−191.

https://doi.org/10.1021/acs.jpcc.6c01502
J. Phys. Chem. C 2026, 130, 7812−7825